Evolution of merging bound states in the continuum at Γ point in parameter space

Qianju Song ⬤,[*] Zao Yi,[†] and Zigang Zhou

School of Mathematics and Physics, Southwest University of Science and Technology, Mianyang 621010, China

Bound states in the continuum (BICs) are resonances with infinite lifetimes, even though they are embedded in the continuous spectrum of free space. Merging multiple BICs can be a promising approach to further improve the Q factors of nearby states over a broad wave-vector range. Previous studies have shown that merging BICs can only appear for specific parameter values of a structure; thus, it is commonly believed that they do not have stability. Here, we analytically study the existence and stability of merging BICs in parameter space, including material and geometric parameters. Specifically, we derive the conditions for the existence of merging-BICs in a system with a periodic plasmonic chain and demonstrate that merging BICs can stably exist when the other parameters are varied. Furthermore, in the momentum-geometric-material space, a BIC surface can be obtained analytically without performing a tedious numerical search of diverging Q factors in a multiple parameter space. Based on this surface, BICs at the Γ point that merge in the momentum space can also merge again in the parameter space by changing the material parameters. The merging BIC with improved Q factor not only covers a broad wave-vector range but also spans a wide geometric parameter space when compared with the original BIC. Our findings provide a different perspective in the investigation of ultrahigh Q factors that substantially enhance light-matter interaction and improve the performance of photonic devices.

I. INTRODUCTION

Bound states in the continuum (BICs) are resonances with infinite lifetimes, even though their corresponding frequencies lie in the continuous spectrum of free space. Although initially demonstrated in custom-constructed potentials in quantum mechanics [1], BICs have attracted extensive attention in classic waves [2–17]. Various mechanisms have been proposed to construct BICs [2–7]. In photonic periodic systems, they can generally be classified into two types: symmetry-protected BICs (usually appearing at highly symmetric points) and accidental BICs. The latter can be validated using the diverging quality (Q) factor through parameter tuning. The unique features of BICs, including their robustness and infinite Q factors, allow them to be used in various applications such as nonlinear optics [8,9], lasers [10], sensors [11,12], and field enhancement [13].

Apart from the their above attractive features, the topological nature of BICs has been investigated [6] and led to further studies of their robustness in momentum space [7,14–20]. The topological nature of BICs enables them to continuously move in the momentum space by varying the system parameters while maintaining the system symmetry. By tuning multiple BICs to the same wave vector, a merging BIC can be formed [7,15,16,19–21]. In practice, the Q factor of an isolated BIC is much lower than the infinity predicted by theory and simulation. This is mainly due to the scattering losses caused by fabrication imperfections or disorders, whereas merging BICs in the momentum space provide a feasible way for

the suppression of scattering losses compared with isolated BICs [16]. However, previous studies have shown that merging BICs are unstable in the momentum space. Recently, merging BICs with $q = 0$ can be found by tuning extra structural parameter [21]. However, the conditions for existence of merging BICs and their stability in the parameter space are not clarified. This lack of clarity is crucial for researching the dynamical evolution of merging BICs in multiple-parameter spaces.

In this work, we employ a plasmonic chain system, which can be analytically solved, to investigate the evolution of merging BICs in the parameter space. Using the coupled-dipole equations, we initially study the existence of merging BICs in the parameter space. Then, using analytical lattice sums, we derive the condition for the existence of merging BICs in such a system without resorting to a numerical search for diverging Q factors. As a result, we find a BIC surface in a 3D space spanned by momentum-geometric-material dimensions, where the merging BICs in the momentum space can merge again in the parameter space by changing the material parameters. It is worth noting that the Q factors of the resulting merging BIC are improved over both a broad geometric parameter range and a wave-vector range compared with those of the original BIC. Merging BICs lead to ultrahigh Q factors in both the parameter and momentum spaces. They can promote the research on topological photonics and have the potential to substantially enhance light-matter interaction, thereby improving the performance of optoelectronic devices.

II. THEORY AND RESULTS

We consider an infinite chain, as shown in Fig. 1(a). This chain consists of plasmonic nanoparticles, which are

---

[*]Corresponding author: qjsong@swust.edu.cn
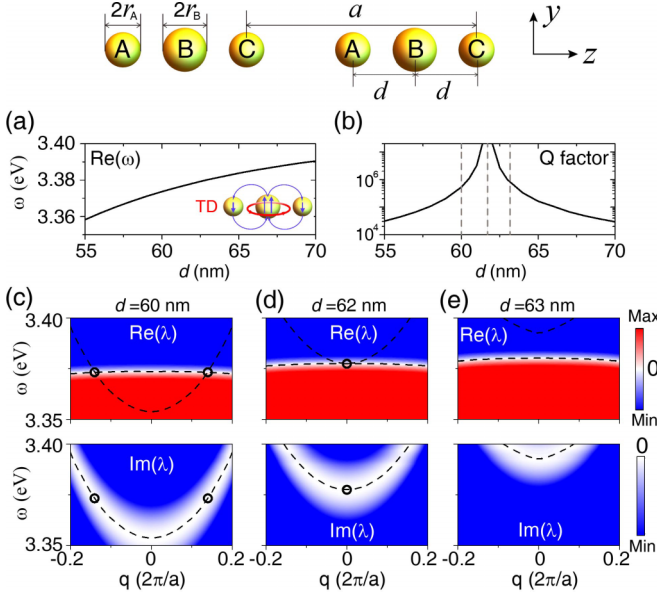[†]Corresponding author: yizaomy@swust.edu.cn

FIG. 1. BICs in 1D plasmonic nanoparticles chains. Top inset: Schematic of a 1D plasmonic chain. The real parts of the resonant frequency and the corresponding Q factor for the Γ point are plotted in (a) and (b), respectively. The resonant mode studied here is dominated by the toroidal dipole, which is schematically shown in (a) as an inset. The Q factor diverges when a BIC is approached. (c) to (e) describe the real part (upper panel) and imaginary part (lower panel) of $\lambda(\omega)$ in the momentum space with different d. With the increase of d, two BICs move towards each other and finally are annihilated. The divergent Q factor in (b) comes from the merging of two accidental BICs in momentum space.

periodically arranged along the z-axis direction. Each unit cell contains three nanoparticles (labeled as A, B, and C). For simplicity, we assume that A and C are identical plasmonic nanoparticles with the radius of r_A, and r_B is the radius of the central nanoparticle B; a is the period of the chain, and d is the distance between two adjacent nanoparticles. Thus, the system maintains mirror symmetry. Each nanoparticle is assumed to be an electric dipole with polarizability $\alpha(\omega) = (3i/2k_0^3)a_1$ assuming $r_{A(B)} \ll \lambda$ (λ is the incident wavelength) and $d > 3r_{A(B)}$ [22]. Here, a_1 is the electric dipole term of the Mie coefficients [23]. The permittivity of metal can be expressed as $\varepsilon(\omega) = 1 - \omega_p^2/\omega(\omega + i\gamma)$, where ω_p is the plasma frequency and γ is the collision frequency of nanoparticles. As we focus on the radiative loss of the system, the intrinsic loss γ is set as zero ($\gamma = 0$) throughout this work. We assume that the dipole moments are perpendicular to the chain; thus, only the transverse modes are considered in the following formulation. It is worth noting that for 1D rotationally symmetric systems, resonant modes can be classified by the azimuthal index m [24]. As for the system considered here, each nanoparticle is assumed to be an electric dipole polarized perpendicularly to the chain axis, so the resonant mode corresponds to the case of $m = 1$.

The response of the plasmonic chain can be obtained through the following approach. When the chain is excited by an external plane wave $\mathbf{E}^{\text{ext}} = \hat{e}_y E_0 e^{i(k_x x + qz)}$, where the electric field is perpendicular to the chain, the system response

can be obtained from the multiple-scattering theory by solving the following equation:

$$
\begin{bmatrix}
\alpha_A^{-1} - S_{AA} & -S_{AB} & -S_{AC} \\
-S_{BA} & \alpha_B^{-1} - S_{BB} & -S_{BC} \\
-S_{CA} & -S_{CB} & \alpha_C^{-1} - S_{CC}
\end{bmatrix}
\begin{bmatrix}
P_A \\
P_B \\
P_C
\end{bmatrix}
=
\begin{bmatrix}
E_A^{\text{ext}} \\
E_B^{\text{ext}} \\
E_C^{\text{ext}}
\end{bmatrix},
$$

(1)

or $M\mathbf{P} = \mathbf{E}$ for convenience. The lattice sums of the Green functions S_{ij} are given in Appendix A. Due to the inversion symmetry of the system, we obtain $\alpha_A = \alpha_C$; S_{ij} have the following properties: $S_{AA} = S_{BB} = S_{CC}$, $S_{AB} = S_{BC}$, and $S_{BA} = S_{CB}$, as shown in Appendix A. It should be pointed out that these lattice sums can be analytically expressed in terms of polylogarithm and Hurwitz-Lerch transcendent functions; therefore, it is possible to study BICs analytically. Furthermore, the material and structure parameters are separately included in $\alpha_{A(B)}$ and S_{ij}. We note that an eigenmode decomposition method can be used to analyze the electromagnetic response of a plasmonic lattice [22,23]. The eigenvalue problem, $M\mathbf{P} = \lambda\mathbf{P}$, is considered instead of the linear response in Eq. (1). If there is an eigenvalue $\lambda = 0$, namely, $M\mathbf{P} = 0$, it will give rise to a nontrivial bound state $\mathbf{P}_0$, i.e., a BIC.

Since we are interested in the resonant states and BICs of the system, we set $\mathbf{E} = 0$ in Eq. (1) and look for the complex frequency solutions of $M\mathbf{P} = 0$ for a certain parameter, i.e., $\omega(\text{param.}) = \omega'(\text{param.}) + \omega''(\text{param.})$. The resonant states supported by the plasmonic chain can be illustrated using symmetry analysis [25]. There are three types of resonant states (see Appendix B for details). One is dominated by the symmetric mode denoted as [1,1,1] with each number representing the dipole moment of the corresponding nanoparticle, where all three dipoles oscillate in phase. Another one is dominated by the antisymmetric mode denoted as [1, 0, −1], where the side dipoles oscillate out of phase. The last one is dominated by another symmetric mode denoted as [1, −2, 1], with the nanoparticles on the two sides oscillating in phase and the central one oscillating out of phase. Therefore, it is dominated by a toroidal dipole mode [25]. The latter two cases correspond to resonant states with high Q factors, so BIC usually appears there. It is well known that a BIC can be indicated by the divergent radiative Q factor due to it being decoupled from the far-field radiation [18,19]. As the intrinsic loss $\gamma = 0$, a resonant state becomes a BIC when its frequency becomes purely real, and the Q factor ω'/ω'' diverges consequently. Here, we focus on the third resonant states that are dominated by the toroidal dipole resonance as illustrated in the inset of Fig. 1(a).

For a given set of geometric and material parameters ($r_A = 18$ nm, $r_B = 1.05 \, r_A$, $a = 240$ nm, and $\omega_p = 6.18$ eV), the variation of the resonance frequency for the Γ point and the corresponding Q factor with respect to parameter d are shown in Figs. 1(a) and 1(b), respectively. Here, we are only interested in the zero-order diffraction region, i.e., $|q| < \omega/c < 2\pi/a - |q|$. The calculated Q factor of the resonant mode goes to infinity at a discrete point ($d = 62$ nm), indicating the existence of a BIC. In fact, this type of BIC is a merging BIC (Γ point) in the momentum space. In Figs. 1(c)–1(e), we plot the real and imaginary parts of the $\lambda(q,\omega)$ for the cases of
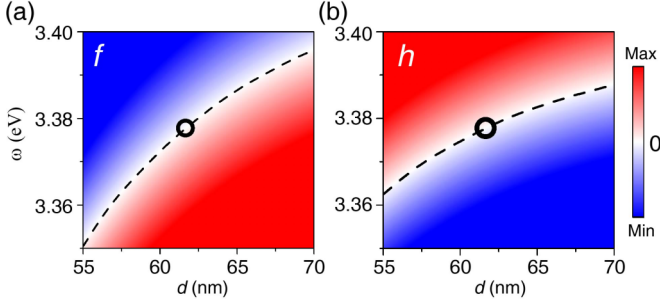
FIG. 2. The existence of merging BICs at the Γ point. The real functions $f(d,\omega)$ and $h(d,\omega)$ defined in Eq. (3) are shown in (a) and (b), respectively. The intersection point of the nodal lines (black lines) of f and h can give rise to a merging BIC.

$d = 60$ nm [Fig. 1(c)], $d = 62$ nm [Fig. 1(d)], and $d = 63$ nm [Fig. 1(e)]. It is clearly seen that as d increases to 62 nm, the two accidental BICs merge at the Γ point, thereby giving a divergent Q factor in Fig. 1(b). The evolution of BICs both in the momentum and parameter spaces will be discussed later.

Next, we analytically derive the conditions for the existence of merging BICs at Γ point in the system. For a BIC with a real frequency solution of Eq. (1), we require that the total dipole moment of the toroidal dipole mode in a unit cell is zero, which gives $\mathbf{P} = [1, -2, 1]^\mathrm{T}$ [25]. This is expected because the superposition of three polarizations in a unit cell does not produce any radiation loss in the far field due to complete field cancellation. Thus, the condition for the existence of BICs becomes the real frequency solutions of

$$f \stackrel{\text{def}}{=} \left(\alpha_A^{-1} - S_{AA}\right) + 2S_{AB} - S_{AC} = 0$$
$$h \stackrel{\text{def}}{=} -2\left(\alpha_B^{-1} - S_{AA}\right) - S_{BA} - S_{AB} = 0$$
$$g \stackrel{\text{def}}{=} \left(\alpha_A^{-1} - S_{AA}\right) + 2S_{BA} - S_{CA} = 0 \qquad (2)$$

However, the conditions $f = 0$, $h = 0$, and $g = 0$ are not completely independent in the determination of BICs. The proof is given in Appendix C. Briefly, the inversion symmetry of the system gives an identity ($f = g$), whereas the time-reversal symmetry gives $f = f^*$ and $h = h^*$; therefore, both f and h are real functions. A rigorous mathematical proof is given in Appendix D. Therefore, the condition for the existence of BICs becomes the solutions of the real equations of

$$f = \mathrm{Re}(f) = 0$$
$$h = \mathrm{Re}(h) = 0. \qquad (3)$$

The real functions f and h are plotted in Figs. 2(a) and 2(b), respectively, in the d–ω plane. The nodal lines of $f(d,\omega)$ and $h(d,\omega)$ are clearly identified and plotted as dashed black lines. These lines intersect at a point (black circle), giving rise to a BIC.

Since the size of the discrete dipoles can be tuned independently, we study the impact of geometric parameters, such as the nanoparticle radii, on a BIC. When the radii of A and B nanoparticles are varied, the real functions $f(d,\omega)$ and $h(d,\omega)$ can be adjusted independently. Figures 3(a) and 3(b) show the dependence of nodal lines of $h(d,\omega)$ and $f(d,\omega)$ on the radius
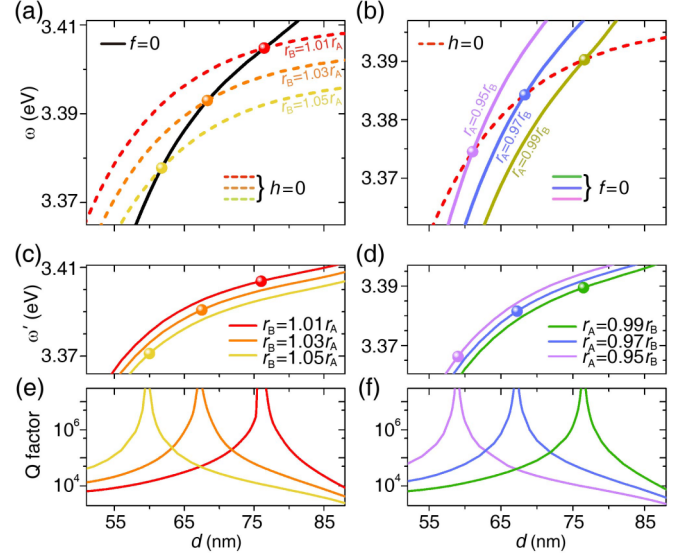

FIG. 3. Evolution of BICs in the geometric parameter space. (a) The three dashed lines denote the nodal lines of real function h for different radius r_B of the central nanoparticle, and the solid black line denotes the nodal line of real function f. (b) The three solid lines denote the nodal lines of f for different radii r_A of the two side nanoparticles, and the dashed red line denotes the nodal line of h. The intersection points of the nodal lines of h and f denoted by the light dots give rise to BICs. The numerically calculated resonance frequency and Q factors are plotted in (c), (d) and (e), (f), respectively. The selected geometric parameters are $r_A = 18$ nm for (a) and $r_B = 19$ nm for (b).

of the center nanoparticle and side nanoparticles, respectively. We observe that $f(d,\omega)$ and $h(d,\omega)$ intersect, giving a real frequency solution of Eq. (3), i.e., a BIC (marked by a light dot). The nodal line of $h(d,\omega)$ shifts to the right and moves the BIC toward the left as the center nanoparticle radius increases, as shown in Fig. 3(a). A similar study can be repeated by varying the radius of the side nanoparticles, as shown in Fig. 3(b). Thus, we observe that the BIC locus follows the nodal line of f when the radius of the center nanoparticle is varied. In contrast, the locus follows the nodal line of h when the side-nanoparticle radius is varied.

The analytical results for the BICs can be verified numerically using the corresponding resonance frequency and Q factors. Figures 3(c) and 3(d) and 3(e) and 3(f) show the resonance frequencies and Q factors simulated using the finite-element method. By either varying the radius of the center nanoparticle or the radius of the side ones, we observe that the shift trends of BICs and the loci of the diverging Q factors are in good agreement with each other.

In addition to the presence of stable BIC with the change of the geometric parameters, a BIC can also stably exist under the variation of material parameter. Here, we assume that the plasma frequency ω_{pB} of nanoparticle B is fixed, and the plasma frequency ω_{pA} of nanoparticle A (as well as nanoparticle C) is varied. Figure 4(a) shows the nodal lines of $f(a,\omega)$ and $h(a,\omega)$ for $\omega_{pA} = 6.185$, 6.188, and 6.1895 eV, which indicates that two BICs gradually approach each other as the plasma frequency increases. They then disappear when
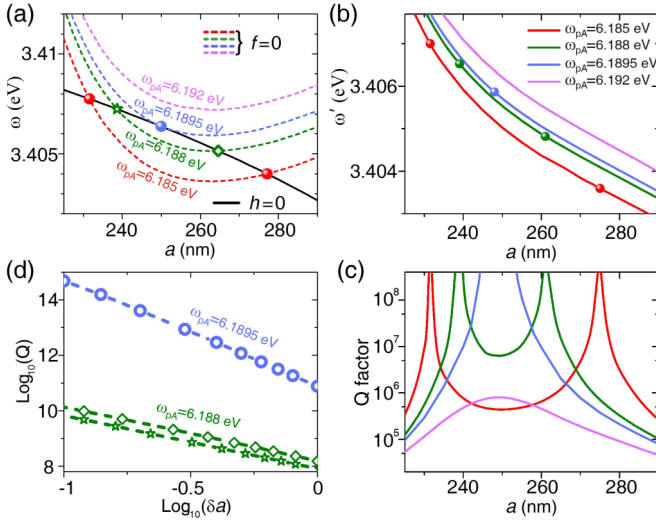
FIG. 4. BICs can merge in the parameter space. (a) The four dashed lines denote the nodal lines of f for different values of plasma frequency ω_p, and the solid black line denotes the nodal line of h. Two intersection points of the nodal lines of f and h give rise to two BICs in the parameter space. The two BICs meet and are annihilated when a critical ω_{pA}^c is reached, above which they suddenly disappear. The numerically calculated resonance frequency and Q factors are plotted in (b) and (c), respectively. The Q factors are illustrated both before ($\omega_{pA} = 6.185$ eV and $\omega_{pA} = 6.188$ eV; red and green lines) and after BIC merging ($\omega_{pA} = 6.192$ eV; purple line). The transition phase ($\omega_{pA}^c = 6.1895$ eV; blue line) corresponds to the merging-BIC configuration, which exhibits considerably higher Q factors than those in the BIC configuration (red and green lines). (d) The divergence rate of the Q-factor rate changes from $Q \propto \delta a^{-2}$ to $Q \propto \delta a^{-4}$ when a critical ω_{pA}^c is approached.

$\omega_{pA} > 6.1895$ eV. Thus, the loci of BICs follow the nodal line of h when ω_{pA} is varied. The corresponding evolution of BICs in momentum space is given in Appendix E. The BICs in Fig. 4(a) correspond exactly to the merging BICs of the momentum space. It is interesting to note that BICs in Fig. 4(a) can merge in the geometric parameter space by varying the material parameters. Here, the selected geometric and material parameters are $r_A = r_B = 18$ nm, $d = 75$ nm, and $\omega_{pB} = 6.18$ eV.

This evolution can be further demonstrated using the corresponding resonance frequency and Q factors shown in Figs. 4(b) and 4(c), respectively. For a critical plasma frequency ($\omega_{pA} = 6.1895$ eV), the Q factors are sufficiently large over a broad geometric range around the Q diverging point, which is a typical feature of merging BICs. By further increasing ω_{pA}, these two BICs annihilate each other and form a quasi-BIC mode, which has a high but nondiverging Q factor. Furthermore, Fig. 4(d) shows the calculated Q factor, which geometrically decays as $Q \sim |a - a_{BIC}|^{-2} = |\delta a|^{-2}$ for the two isolated BICs indicated by a green diamond and a star, respectively, in Fig. 4(a). When these two BICs merge, as $Q \sim |\delta a|^{-4}$ (blue line), the decay rate of the Q factor away from the BIC is improved. The nearby Q factor is several orders of magnitude higher than that of the isolated BICs in the geometric parameter space when the material parameters are varied to produce the merging BIC.
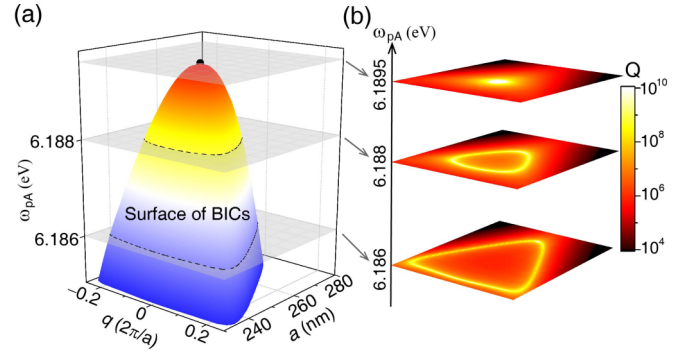

FIG. 5. Evolution of BICs in the parameter space. (a) The BICs in the q-a-ω_{pA} space form a closed surface. The contour of BICs in the q–a space shrinks with the increase of ω_{pA} and then reduces to a single point when $\omega_{pA} = \omega_{pA}^c$, above which the merging BIC disappears. (b) Numerically obtained slices at three values of ω_{pA}. Distributions of the Q factor corresponding to $\omega_{pA} = 6.186$ eV, $\omega_{pA} = 6.188$ eV, and $\omega_{pA}^c = 6.1895$ eV are presented.

The preceding examples illustrate the stability of BICs under varying conditions, encompassing changes in material and geometric parameters. We further demonstrate the evolution of BICs in the momentum-geometric-material space. As shown in Fig. 5(a), we vary the momentum q, chain period a, and plasma frequency ω_{pA}. A surface of BICs is obtained analytically. The trace of BICs form a closed loop in q-a space for a fixed ω_{pA}. This means that when the other parameters are fixed, as a increases from a small value (<230 nm here), a BIC is generated at the Γ point, and soon splits into two BICs moving away from the Γ point. Then, the two BICs move back toward the Brillouin-zone center. Finally, they annihilate at the Γ point. According to the contour of BICs, the loop in Fig. 5(a) shrinks when ω_{pA} increases. When a critical value is approached, the loop of BICs reduces to a single BIC point; beyond this critical value, it disappears. It is worth noting that all the BICs described in Fig. 1 to Fig. 4 are merging BICs in momentum space, whereas in Fig. 5, only the BICs with $q = 0$ correspond to merging BICs, while the others are accidental BICs.

For further verification, the simulated Q factors, evaluated in the q-a space using the finite-element method, are shown in Fig. 5(b). A clear loop of BICs with a diverging Q factor is observed. The loop reduces to a single point and forms a merging BIC when a critical ω_{pA} is reached, as shown at the top plane of Fig. 5(b). It is worth emphasizing that the off-Γ BICs mentioned previously are based on the dipole approximation [19]. If other multipoles, although they are extremely weak as their size is much smaller than the wavelength, are taken into account, the off-Γ BICs will turn into quasi-BICs with high Q factors. In this case, the TE and TM components of the resonant mode are fully coupled [24] and it is very difficult to diminish the two radiations simultaneously, whereas the at-Γ merging BICs are all bona fide BICs due to the TM channel being closed at the Γ point [24]. It is worth noting that the merging BICs investigated here are rather different from those reported in previous studies [5,9,15,16,19]. They not only exhibit a quartic behavior of Q^{-1} in the momentum space but also in the parameter space, whereas the previously

reported behavior of merging BICs is only enhanced in the momentum space. The merging of BICs in both the parameter and momentum spaces leads to enhanced Q factors for the nearby states, resulting in improved performance in practical applications.

III. CONCLUSION

In summary, we demonstrated that a plasmonic chain provides an analytically solvable model for merging BICs. We also demonstrated that merging BICs can stably exist under changes in extra parameters, including the material and geometric ones. By varying the material parameters, the BICs that merge in the momentum space can merge again in the parameter space. Furthermore, a BIC surface in the momentum-geometric-material space is obtained analytically without resorting to a tedious numerical search for diverging Q factors in a multiple-parameter space. The vertex of the BIC surface corresponds to a merging BIC in both parameter and momentum spaces. It is worth noting that the Q factors are enhanced over a broad range of geometric parameters and wave vectors at this surface vertex compared to the original BIC. Merging BICs in both the parameter and momentum spaces lead to extremely high Q factors, enrich the investigation of topological photonics, and are potentially useful in nonlinear optics and lasers by improving the performance of optoelectronic devices.

APPENDIX A: COUPLED DIPOLE EQUATION FOR PLASMONIC CHAINS

Let us consider a periodic plasmonic lattice as specified in the upper inset of Fig. 1 of the main text. For simplicity, a TE-polarized incidence with the electric field perpendicular to the chain is considered: $\mathbf{E}^{\text{ext}} = \hat{e}_y E_0 e^{i(k_x x + qz)}$ and $\mathbf{E}_0 = (0, E_0, 0)$. Only the transverse mode is considered, i.e., $\mathbf{P}_{A,B} = (0, p_{A,B}, 0)$. Using Bloch theorem, the coupled-dipole equations for the chain can be written as

$$p_A = \alpha_A \left(E_A^{\text{ext}} + \sum_{n \neq 0} G(na) p_{n,A} + \sum_n G(na+d) p_{n,B} + \sum_n G(na+2d) p_{n,C} \right)$$

$$p_B = \alpha_B \left(E_B^{\text{ext}} + \sum_{n \neq 0} G(na) p_{n,B} + \sum_n G(na-d) p_{n,A} + \sum_n G(na+d) p_{n,C} \right)$$

$$p_C = \alpha_C \left(E_C^{\text{ext}} + \sum_{n \neq 0} G(na) p_{n,C} + \sum_n G(na-2d) p_{n,A} + \sum_n G(na-d) p_{n,B} \right),$$

where G is Green's function for electric dipoles. The above coupled-dipole equations can be reexpressed as

$$\begin{bmatrix} \alpha_A^{-1} - S_{AA} & -S_{AB} & -S_{AC} \\ -S_{BA} & \alpha_B^{-1} - S_{BB} & -S_{BC} \\ -S_{CA} & -S_{CB} & \alpha_C^{-1} - S_{CC} \end{bmatrix} \begin{bmatrix} P_A \\ P_B \\ P_C \end{bmatrix} = \begin{bmatrix} E_A^{\text{ext}} \\ E_B^{\text{ext}} \\ E_C^{\text{ext}} \end{bmatrix}, \tag{A1}$$

i.e., Eq. (1) in the main text, or in a more compact form: $M\mathbf{P} = \mathbf{E}$, where α is the polarizability of the nanoparticles, and the lattice sums S_{ij} of Green's functions have the following forms:

$$S_{AA} = S_{BB} = S_{CC} = \sum_{n \neq 0} g(na) e^{iqna} \quad S_{AB} = S_{BC} = \sum_n g(na+d) e^{iqna} \quad S_{AC} = \sum_n g(na+2d) e^{iqna}$$

$$S_{BA} = S_{CB} = \sum_n g(na-d) e^{iqna} \quad S_{CA} = \sum_n g(na-2d) e^{iqna}. \tag{A2}$$

The above the lattice sums S_{ij} can be reexpressed as

$$S_{AA} = S_{BB} = S_{BB} = k_0^3 \sum_{n \neq 0} \left(\frac{1}{k_0 |na|} + i \frac{1}{k_0^2 |na|^2} - \frac{1}{k_0^3 |na|^3} \right) e^{ik_0 |na|} e^{iqna}$$

$$S_{AB} = S_{BC} = k_0^3 \sum_n \left(\frac{1}{k_0 |na+d|} + i \frac{1}{k_0^2 |na+d|^2} - \frac{1}{k_0^3 |na+d|^3} \right) e^{ik_0 |na+d|} e^{iqna}$$

$$S_{BA} = S_{CB} = k_0^3 \sum_n \left(\frac{1}{k_0|na-d|} + i\frac{1}{k_0^2|na-d|^2} - \frac{1}{k_0^3|na-d|^3} \right) e^{ik_0|na-d|} e^{iqna}$$

$$S_{AC} = k_0^3 \sum_n \left(\frac{1}{k_0|na+2d|} + i\frac{1}{k_0^2|na+2d|^2} - \frac{1}{k_0^3|na+2d|^3} \right) e^{ik_0|na+2d|} e^{iqna}$$

$$S_{CA} = k_0^3 \sum_n \left(\frac{1}{k_0|na-2d|} + i\frac{1}{k_0^2|na-2d|^2} - \frac{1}{k_0^3|na-2d|^3} \right) e^{ik_0|na-2d|} e^{iqna}. \tag{A3}$$

The lattice sums in Eq. (A3) can be expressed in terms of certain special functions:

$$S_{AA} = S_{BB} = S_{CC} = k_0^3 \left(\frac{L_1}{k_0 a} + i\frac{L_2}{k_0^2 a^2} - \frac{L_3}{k_0^3 a^3} \right)$$

$$S_{AB} = S_{BC} = k_0^3 \left(\frac{\Phi_{1,1}}{k_0 a} + i\frac{\Phi_{1,2}}{k_0^2 a^2} - \frac{\Phi_{1,3}}{k_0^3 a^3} - \Phi_1 \right)$$

$$S_{BA} = S_{CB} = k_0^3 \left(\frac{\Phi_{-1,1}}{k_0 a} + i\frac{\Phi_{-1,2}}{k_0^2 a^2} - \frac{\Phi_{-1,3}}{k_0^3 a^3} - \Phi_1 \right)$$

$$S_{AC} = k_0^3 \left(\frac{\Phi_{2,1}}{k_0 a} + i\frac{\Phi_{2,2}}{k_0^2 a^2} - \frac{\Phi_{2,3}}{k_0^3 a^3} - \Phi_2 \right)$$

$$S_{CA} = k_0^3 \left(\frac{\Phi_{-2,1}}{k_0 a} + i\frac{\Phi_{-2,2}}{k_0^2 a^2} - \frac{\Phi_{-2,3}}{k_0^3 a^3} - \Phi_2 \right), \tag{A4}$$

where

$$L_n = Li_n\left(e^{i(k_0-q)a}\right) + Li_n\left(e^{i(k_0+q)a}\right)$$

$$\Phi_{m,n} = \Phi\left(e^{i(k_0+q)a}, n, m\frac{d}{a}\right) e^{imk_0 d}$$

$$\qquad + \Phi\left(e^{i(k_0-q)a}, n, -m\frac{d}{a}\right) e^{-imk_0 d}$$

$$\Phi_m = \left(-\frac{1}{k_0(md)} + i\frac{1}{k_0^2(md)^2} + \frac{1}{k_0^3(md)^3} \right) e^{-ik_0(md)}.$$

And, $Li_n(x)$ and $\Phi(z, s, a)$ are the polylogarithm function and the Hurwitz-Lerch transcendent function, respectively.

By changing the variable from n to $-n$ in Eq. (A3), it is straightforward to show that the lattice sums in Eq. (A3) satisfy the following symmetry relations:

$$S_{AA(BB,CC)}(-q, \omega) = S_{AA(BB,CC)}(q, \omega)$$

$$S_{AB(AC,BC)}(-q, \omega) = S_{BA(CA,CB)}(q, \omega), \tag{A5}$$

or equivalently,

$$M(-q, \omega) = M^{\mathrm{T}}(q, \omega). \tag{A6}$$

Equation (A6) is consistent with the inversion symmetry of the plasmonic chain. Under the inversion along the z direction (axis of the chain), $z \rightarrow -z$; this yields nanoparticle $A \rightarrow$ nanoparticle C, and leads to $q \rightarrow -q$ for the Bloch eigenstate.

For the M matrix, the inversion gives

$$M(-q, \omega) = \sigma_x M(q, \omega) \sigma_x,$$

which gives rise to Eqs. (A5) and (A6).

APPENDIX B: THREE TYPES OF RESONANT STATES SUPPORTED BY SYSTEM

Under the dipole approximation, the transverse plasmonic modes supported by the 1D chain [Fig. 6(a)], denoted as $\mathbf{P} = [P_A, P_B, P_C]^{\mathrm{T}}$, can be decomposed into three orthogonal bases: $\mathbf{A} \sim [1, 0, -1]^{\mathrm{T}}$, $\mathbf{S}_1 \sim [1, 1, 1]^{\mathrm{T}}$, and $\mathbf{S}_2 \sim [1, -2, 1]^{\mathrm{T}}$ with $\mathbf{A}$ antisymmetric and $\mathbf{S}_1$, $\mathbf{S}_2$ symmetric (see Ref. [25]). The so-called toroidal dipole resonance is mainly supported by the $\mathbf{S}_2$ mode, where the two side dipoles oscillate in phase while the central one oscillates out of phase. More specifically, because the dipoles can act as current elements (blue arrows) in Fig. 6(b), this model mimics the toroidal current configuration shown in Fig. 6(a); therefore, a toroidal
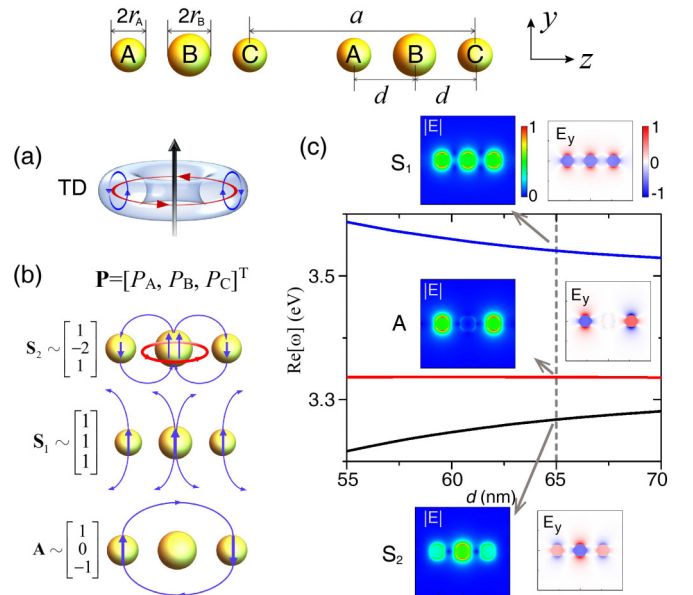

FIG. 6. Top inset: Schematic of a 1D plasmonic chain. (a) Schematics of a typical toroidal dipole moment. (b) For the transverse mode we consider the system dominated by three type of modes, antisymmetric mode (**A** mode), symmetric modes (**S**₁ and **S**₂). Toroidal dipole moment is dominated by **S**₂ mode. And, the equivalent current outflows from the center nanoparticle and flows back through the side ones. (c) The real parts of the resonant frequency for the Γ point. The spatial profiles of the $|\mathbf{E}|$ and E_y for the three resonant mode are shown in the corresponding insets.
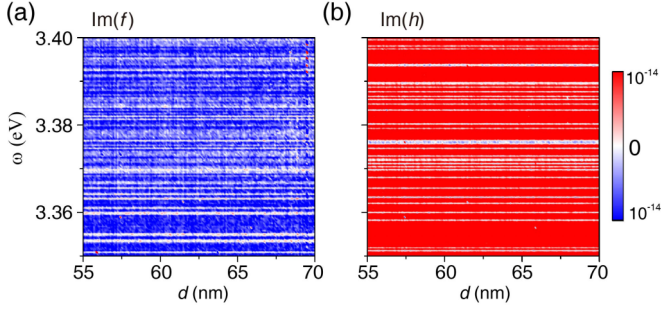
FIG. 7. Im(f) and Im(h) are illustrated in the d-ω space. This shows that f and h are two real functions.

dipole is induced. In our paper, only the modes dominated by toroidal dipole resonance are studied.

At the same time, we also give the numerical calculation about the resonant mode vs the center-to-center distance d as shown in Fig. 6(c). We take $d = 65$ nm as an example and give the spatial field profiles in the near field for the three resonant modes, respectively. It can be clearly seen that the lowest-frequency mode we are concerned about is dominated by toroidal dipole moment.

APPENDIX C: RIGOROUS PROOF OF EXISTENCE OF MERGING BICS

From Eqs. (A1) and (A5), the matrix M for the chain in our main text can be expressed as

$$M = \begin{bmatrix} \alpha_A^{-1} - S_{AA} & -S_{AB} & -S_{AC} \\ -S_{BA} & \alpha_B^{-1} - S_{AA} & -S_{AB} \\ -S_{CA} & -S_{BA} & \alpha_A^{-1} - S_{AA} \end{bmatrix}, \quad \text{(C1)}$$

where α_0 contains the term of radiation loss. The inverse polarizability $\alpha_{A(B)}^{-1}(\omega) = \frac{1}{r_{A(B)}^3}(\frac{\omega_{pA(B)}^2 - 3\omega^2}{\omega_{pA(B)}^2}) - \frac{2i}{3}k_0^3$, where the imaginary part denotes the radiation loss [26] and $k_0 = \omega/c$, with c being the light speed in vacuum. We first consider the Brillouin-zone center, i.e., $q = 0$. A real frequency solution of $M\mathbf{P}_0 = 0$ gives rise to a BIC with $\mathbf{P}_0$ being the eigenstate of BIC. Since a BIC does not radiate, the two side-dipole moments in the cell-periodic wave function must be out of phase with the center-dipole moment in order to produce complete destructive interference of the radiation in the far field. Thus, we can write

$$\mathbf{P}_0 = \begin{bmatrix} p_A \\ p_B \\ p_C \end{bmatrix} = \frac{1}{\sqrt{6}}\begin{bmatrix} 1 \\ -2 \\ 1 \end{bmatrix}. \quad \text{(C2)}$$

Substituting Eqs. (C1) and (C2) into $M\mathbf{P}_0 = 0$, we obtain the condition for a BIC as the real frequency solution of the following equations:

$$(\alpha_A^{-1} - S_{AA}) + 2S_{AB} - S_{AC} = 0 \stackrel{\text{def}}{=} f$$

$$-2(\alpha_B^{-1} - S_{AA}) - S_{BA} - S_{AB} = 0 \stackrel{\text{def}}{=} h$$

$$(\alpha_A^{-1} - S_{AA}) + 2S_{BA} - S_{CA} = 0 \stackrel{\text{def}}{=} g, \quad \text{(C3)}$$
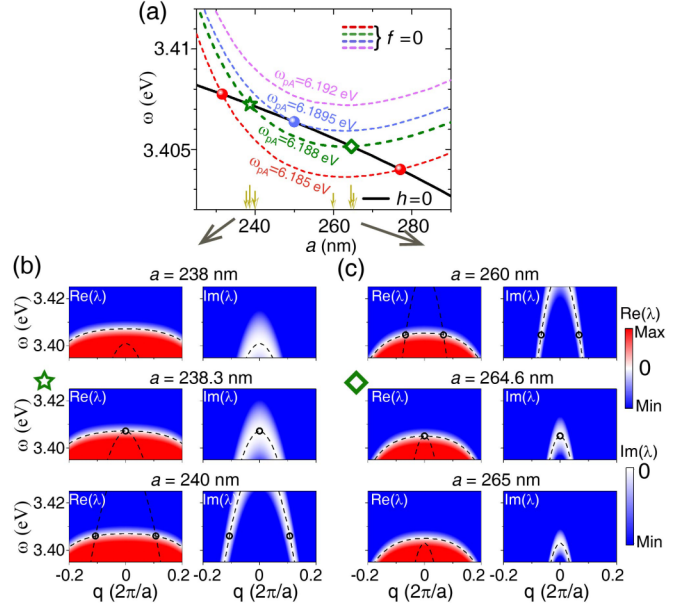

FIG. 8. (a) The intersection points of the nodal lines of f and h give rise to the merging BICs. The real and imaginary parts of $\lambda(\omega)$ at different period a [emphasized by six golden arrows in (a)] are plotted in (b) and (c), which give the evolution of BICs at the vicinity of the two merging BICs indicated by the green star and green diamond in (a). The above BICs comes from the merging of two accidental BICs in momentum space [middle panel of (b) and (c)].

which is Eq. (2). We have already proved the identity $f = g$ from inversion symmetry, i.e., Eq. (A6). Here, we will prove the identity $f = f^*$ and $h = h^*$ for the BIC at $q = 0$ by applying time-reversal operation on $M\mathbf{P} = 0$, i.e.,

$$\Theta M \Theta^{-1} \Theta \mathbf{P} = M^* \mathbf{P}^* = 0,$$

where Θ is the time-reversal operator. Since we consider the $q = 0$ and the frequency is real at the BIC, we have $\mathbf{P}^* = \mathbf{P}_0$. The Bloch wave function of this BIC also has the form in Eq. (C2). As a result, we have the following identities:

$$(\alpha_A^{-1} - S_{AA})^* + 2S_{AB}^* - S_{AC}^*$$

$$= (\alpha_A^{-1} - S_{AA}) + 2S_{AB} - S_{AC} = 0$$

$$- 2(\alpha_B^{-1} - S_{AA})^* - S_{BA}^* - S_{AB}^*$$

$$= -2(\alpha_B^{-1} - S_{AA}) - S_{BA} - S_{AB} = 0,$$

from which, we obtain

$$f = f^* \quad \text{and} \quad h = h^*, \quad \text{(C4)}$$

i.e., f and h are two real functions whose solution determine the position BIC.

In fact, Eq. (C4) holds not only at BICs, but in general in the region of zeroth-order diffraction and the whole range of parameter spaces in which we are interested. To prove this, we need to prove that f and h are two real-valued functions. To prove the above, we need to rely on the following theorems:

The following result always satisfied for the region of zeroth-order diffraction, $b = d/a \in (0, 1)$,

$$-\sum_{n \neq 0} \frac{\sin|nx|}{|nx|} + \sum_n \frac{\sin|(n+b)x|}{|(n+b)x|} = 1$$

$$-\sum_{n \neq 0} \frac{\cos|nx|}{|nx|^2} + \sum_n \frac{\cos|(n+b)x|}{|(n+b)x|^2} = \frac{1}{x^2}\left(\frac{1}{b^2} - \frac{\pi^2}{3} + 2g(b)\right) - \frac{1}{2},$$

$$\sum_{n \neq 0} \frac{\sin|nx|}{|nx|^3} - \sum_n \frac{\sin|(n+b)x|}{|(n+b)x|^3} = \frac{1}{x^2}\left(\frac{\pi^2}{3} - \frac{1}{b^2} - 2g(b)\right) + \frac{1}{6}, \tag{C5}$$

where $g(b) = \sum_{n=1}^{\infty} \frac{1}{(n+b)^2}$ and $x = k_0 a$. The above theorems have been proved in Ref. [27]. The rigorous mathematical proof of $f = f^*$ and $h = h^*$ is given in Appendix D. A numerical verification is shown in Fig. 7.

APPENDIX D: RIGOROUS MATHEMATICAL PROOF OF $f = f^*$ AND $h = h^*$

Substituting Eq. (A3) into (C3), the f and h function can be reexpressed as

$$f = \alpha_A^{-1} - k_0^3 \sum_{n \neq 0}\left(\frac{1}{k_0|na|} + i\frac{1}{k_0^2|na|^2} - \frac{1}{k_0^3|na|^3}\right)e^{ik_0|na|} + 2k_0^3 \sum_n\left(\frac{1}{k_0|na+d|} + i\frac{1}{k_0^2|na+d|^2} - \frac{1}{k_0^3|na+d|^3}\right)e^{ik_0|na+d|}$$

$$- k_0^3 \sum_n\left(\frac{1}{k_0|na+2d|} + i\frac{1}{k_0^2|na+2d|^2} - \frac{1}{k_0^3|na+2d|^3}\right)e^{ik_0|na+2d|},$$

$$h = -2\alpha_B^{-1} + 2k_0^3 \sum_{n \neq 0}\left(\frac{1}{k_0|na|} + i\frac{1}{k_0^2|na|^2} - \frac{1}{k_0^3|na|^3}\right)e^{ik_0|na|} - k_0^3 \sum_n\left(\frac{1}{k_0|na-d|} + i\frac{1}{k_0^2|na-d|^2} - \frac{1}{k_0^3|na-d|^3}\right)e^{ik_0|na-d|}$$

$$- k_0^3 \sum_n\left(\frac{1}{k_0|na+d|} + i\frac{1}{k_0^2|na+d|^2} - \frac{1}{k_0^3|na+d|^3}\right)e^{ik_0|na+d|}. \tag{D1}$$

First, we prove that the imaginary part of h is zero. The imaginary part of h can be expressed as

$$\text{Im}(h) = \frac{4}{3}k_0^3 + 2k_0^3 \sum_{n \neq 0}\left(\frac{\sin|nx|}{|nx|} + \frac{\cos|nx|}{|nx|^2} - \frac{\sin|nx|}{|nx|^3}\right) - k_0^3 \sum_n\left(\frac{\sin|(n-b)x|}{|(n-b)x|} + \frac{\cos|(n-b)x|}{|(n-b)x|^2} - \frac{\sin|(n-b)x|}{k_0^3|(n-b)x|^3}\right),$$

$$- k_0^3 \sum_n\left(\frac{\sin|(n+b)x|}{|(n+b)x|} + \frac{\cos|(n+b)x|}{|(n+b)x|^2} - \frac{\sin|(n+b)x|}{|(n+b)x|^3}\right), \tag{D2}$$

where $x = k_0 a$ and $b = d/a$.

We reformulate the summation in terms of the power of the denominator in Eq. (D2) as follows. Substituting Eq. (C5) into (D2), we obtain

$$\text{Im}(h) = \frac{4}{3}k_0^3 + 2k_0^3 \sum_{n \neq 0}\left(\frac{\sin|nx|}{|nx|} + \frac{\cos|nx|}{|nx|^2} - \frac{\sin|nx|}{|nx|^3}\right) - k_0^3 \sum_n\left(\frac{\sin|(n+b)x|}{|(n+b)x|} + \frac{\cos|(n+b)x|}{|(n+b)x|^2} - \frac{\sin|(n+b)x|}{k_0^3|(n+b)x|^3}\right)$$

$$- k_0^3 \sum_n\left(\frac{\sin|(n+2b)x|}{|(n+2b)x|} + \frac{\cos|(n+2b)x|}{|(n+2b)x|^2} - \frac{\sin|(n+2b)x|}{|(n+2b)x|^3}\right)$$

$$= \frac{4}{3}k_0^3 - 2k_0^3 - 2\left[\frac{1}{x^2}\left(\frac{1}{b^2} - \frac{\pi^2}{3} + 2g(b)\right) - \frac{1}{2}\right]k_0^3 - 2\left[\frac{1}{x^2}\left(\frac{\pi^2}{3} - \frac{1}{b^2} - 2g(b)\right) + \frac{1}{6}\right]k_0^3 = 0. \tag{D3}$$

Below, we prove that the imaginary part of f in Eq. (D1) is zero. To prove this, we need to rely on the following theorems [27]:

$$\sum_{n \neq 0} \frac{\sin|nx|}{|nx|} = \frac{\pi}{x} - 1, \quad \sum_n \frac{\sin|(n+b)x|}{|(n+b)x|} = \frac{\pi}{x}$$

$$\sum_{n \neq 0} \frac{\cos|nx|}{|nx|^2} = \frac{1}{x^2}\left(\frac{x^2}{2} - \pi x + \frac{\pi^2}{3}\right), \quad \sum_n \frac{\cos|(n+b)x|}{|(n+b)x|^2} = \frac{1}{x^2}\left(\frac{1}{b^2} - \pi x + 2g(b)\right)$$

$$\sum_{n \neq 0} \frac{\sin|nx|}{|nx|^3} = \frac{1}{x^3}\left(-\frac{\pi}{2}x^2 + \frac{\pi^2}{3}x\right) + \frac{1}{6}, \quad \sum_n \frac{\sin|(n+b)x|}{|(n+b)x|^3} = \frac{1}{x^3}\left(-\frac{\pi}{2}x^2 + \left(2g(b) + \frac{1}{b^2}\right)x\right). \tag{D4}$$

The imaginary part of f can be expressed as

$$\mathrm{Im}(f) = -\frac{2}{3}k_0^3 - k_0^3 \sum_{n\neq 0}\left(\frac{\sin|nx|}{|nx|} + \frac{\cos|nx|}{|nx|^2} - \frac{\sin|nx|}{|nx|^3}\right) + 2k_0^3 \sum_n \left(\frac{\sin|(n+b)x|}{|(n+b)x|} + \frac{\cos|(n+b)x|}{|(n+b)x|^2} - \frac{\sin|(n+b)x|}{k_0^3|(n+b)x|^3}\right)$$
$$- k_0^3 \sum_n \left(\frac{\sin|(n+2b)x|}{|(n+2b)x|} + \frac{\cos|(n+2b)x|}{|(n+2b)x|^2} - \frac{\sin|(n+2b)x|}{|(n+2b)x|^3}\right). \tag{D5}$$

We reformulate the summation in terms of the power of the denominator in Eq. (D5) as follows:

$$\mathrm{Im}(f) = -\frac{2}{3}k_0^3 - k_0^3 \sum_{n\neq 0}\left(\frac{\sin|nx|}{|nx|} + \frac{\cos|nx|}{|nx|^2} - \frac{\sin|nx|}{|nx|^3}\right) + k_0^3 \sum_n \left(\frac{\sin|(n+b)x|}{|(n+b)x|} + \frac{\cos|(n+b)x|}{|(n+b)x|^2} - \frac{\sin|(n+b)x|}{k_0^3|(n+b)x|^3}\right)$$
$$= -\frac{2}{3}k_0^3 + k_0^3 + k_0^3\left(\frac{1}{x^2}\left(\frac{1}{b^2} - \frac{\pi^2}{3} + 2g(b)\right) - \frac{1}{2}\right) + k_0^3\left(\frac{1}{x^2}\left(\frac{\pi^2}{3} - \frac{1}{b^2} - 2g(b)\right) + \frac{1}{6}\right) = 0. \tag{D6}$$

Finally, from (D3) and (D6), we get that f and h are two real-valued functions for $b = d/a \in (0, 1)$.

APPENDIX E: EVOLUTION OF BIC IN MOMENTUM SPACE

As shown in Fig. 8, we also give the evolution of BIC in momentum space of Fig. 4. Here we take the plasma frequency equal to 6.188 eV as an example. When period a is 238.3 nm (green star) and 264.6 nm (green diamond), respectively, the modes at the Γ point correspond exactly to the BIC modes. Near $a = 238.3$ nm and $a = 264.6$ nm, the real and imaginary parts of λ in the q-ω space for several values of a [emphasized by six golden arrows in Fig. 8(a)] are plotted in Figs. 8(b) and 8(c), respectively. It can be clearly seen that the BICs (green star and green diamond) in Fig. 8(a) correspond exactly to the merging BICs in the momentum space.

[1] J. von Neumann and E. Wigner, Über merkwürdige diskrete Eigenwerte, Phys. Z. **30**, 465 (1929).

[2] C. W. Hsu, B. Zhen, A. D. Stone, J. D. Joannopoulos, and M. Soljačić, Bound states in the continuum, Nat. Rev. Mater. **1**, 16048 (2016).

[3] H. Friedrich and D. Wintgen, Interfering resonances and bound states in the continuum, Phys. Rev. A **32**, 3231 (1985).

[4] E. N. Bulgakov and A. F. Sadreev, Formation of bound states in the continuum for a quantum dot with variable width, Phys. Rev. B **83**, 235321 (2011).

[5] E. N. Bulgakov and D. N. Maksimov, Topological bound states in the continuum in arrays of dielectric spheres, Phys. Rev. Lett. **118**, 267401 (2017).

[6] B. Zhen, C. W. Hsu, L. Lu, A. D. Stone, and M. Soljačić, Topological nature of optical bound states in the continuum, Phys. Rev. Lett. **113**, 257401 (2014).

[7] Q. Jiang, P. Hu, J. Wang, D. Han, and J. Zi, General bound states in the continuum in momentum space, Phys. Rev. Lett. **131**, 013801 (2023).

[8] Z. Liu, Y. Xu, Y. Lin, J. Xiang, T. Feng, Q. Cao, J. Li, S. Lan, and J. Liu, High-Q quasibound states in the continuum for nonlinear metasurfaces, Phys. Rev. Lett. **123**, 253901 (2019).

[9] L. Yuan and Y. Y. Lu, Bound states in the continuum on periodic structures surrounded by strong resonances, Phys. Rev. A **97**, 043828 (2018).

[10] C. Huang, C. Zhang, S. Xiao, Y. Fan Y.Wang, Y. Liu, N. Zhang, G. Qu, H. Ji, J. Han, L. Ge, Y. Kivshar, and Q. Song, Ultrafast control of vortex microlasers, Science **367**, 1018 (2020).

[11] M. Zhang and X. D. Zhang, Ultrasensitive optical absorption in graphene based on bound states in the continuum, Sci. Rep. **5**, 8266 (2015).

[12] B. Hou, Z. Li, L. He, Z. Yi, Q. Song, H. Yang, and H. Li, Enhanced quasi-BIC refractive index sensing based on controlling the Fermi energy of Dirac semimetal metasurface, Opt. Laser Technol. **164**, 109537 (2023).

[13] X. Wang, J. Duan, W. Chen, C. Zhou, T. Liu, and S. Y. Xiao, Controlling light absorption of graphene at critical coupling through magnetic dipole quasi-bound states in the continuum resonance, Phys. Rev. B **102**, 155432 (2020).

[14] W. Liu, B. Wang, Y. Zhang, J. Wang, M. Zhao, F. Guan, X. Liu, L. Shi, and J. Zi, Circularly polarized states spawning from bound states in the continuum, Phys. Rev. Lett. **123**, 116104 (2019).

[15] M. Kang, S. Zhang, M. Xiao, and H. Xu, Merging bound states in the continuum at off-high symmetry points, Phys. Rev. Lett. **126**, 117402 (2021).

[16] J. Jin, X. Yin, L. Ni, M. Soljačić, B. Zhen, and C. Peng, Topologically enabled ultrahigh-Q guided resonances robust to out-of-plane scattering, Nature (London) **574**, 501 (2019).

[17] T. Yoda and M. Notomi, Generation and annihilation of topologically protected bound states in the continuum and circularly polarized states by symmetry breaking, Phys. Rev. Lett. **125**, 053902 (2020).

[18] Y. Zeng, G. Hu, K. Liu, Z. Tang, and C. W. Qiu, Dynamics of topological polarization singularity in momentum space, Phys. Rev. Lett. **127**, 176101 (2021).

[19] Q. Song, Z. Yi, H. Xiang, and D. Han, Dynamics and asymmetric behavior of loss-induced bound states in the continuum in momentum space, Phys. Rev. B **107**, 165142 (2023).

[20] X. Qi, J. Wu, F. Wu, M. Ren, Q. Wei, Y. Wang, and H. Chen, Steerable merging bound states in the continuum on a

quasi-flatband of photonic crystal slabs without breaking symmetry, Photon. Res. **11**, 1262 (2023).

[21] L. Yuan and Y. Y. Lu, Propagating Bloch modes above the lightline on a periodic array of cylinders, J. Phys. B: At. Mol. Opt. Phys. **50**, 05LT01 (2017).

[22] W. H. Weber and G. W. Ford, Propagation of optical excitations by dipolar interactions in metal nanoparticle chains, Phys. Rev. B **70**, 125429 (2004).

[23] K. H. Fung and C. T. Chan, Plasmonic modes in periodic metal nanoparticle chains: A direct dynamic eigenmode analysis, Opt. Lett. **32**, 973 (2007).

[24] N. Zhang and Y. Y. Lu, Robust and non-robust bound states in the continuum in rotationally symmetric periodic waveguides, Opt. Express **31**, 15810 (2023).

[25] M. Gong, P. Hu, Q. Song, H. Xiang, and D. Han, Bound states in the continuum from a symmetric mode with a dominant toroidal dipole resonance, Phys. Rev. A **105**, 033504 (2022).

[26] V. A. Markel, Antisymmetrical optical states, J. Opt. Soc. Am. B **12**, 1783 (1995).

[27] Q. J. Song, J. Hu, S. Dai, C. Zheng, D. Han, J. Zi, Z. Q. Zhang, and C. T. Chan, Coexistence of a new type of bound state in the continuum and a lasing threshold mode induced by PT symmetry, Sci. Adv. **6**, eabc1160 (2020).